Appl Phys A (2009) 95: 523–536
DOI 10.1007/s00339-008-4936-x

Applied Physics A
Materials Science & Processing

Assembly of sol–gel-grown Li_xCoO_2 nanocrystals through electromagnetic irradiation

Mahua Das · R. Ranjith · C. Bittencourt · S.B. Krupanidhi · J.J. Pireaux · S.A. Shivashankar

Received: 25 August 2008 / Accepted: 3 September 2008 / Published online: 15 November 2008

Abstract We report the fabrication of assembled nanostructures from the pre-synthesized nanocrystals building blocks through optical means of exciton formation and dissociation. We demonstrate that Li_xCoO_2 nanocrystals assemble to an acicular architecture, upon prolonged exposure to ultraviolet–visible radiation emitted from a 125 W mercury vapor lamp, through intermediate excitation of excitons. The results obtained in the present study clearly show how nanocrystals of various materials with band gaps appropriate for excitations of excitons at given optical wavelengths can be assembled to unusual nanoarchitectures through illumination with incoherent light sources. The disappearance of exciton bands due to Li_xCoO_2 phase in the optical spectrum of the irradiated film comprising acicular structure is consistent with the proposed mechanism of exciton dissociation in the observed light-induced assembly process. The assembly process occurs through attractive Coulomb interactions between charged dots created upon exciton dissociation. Our work presents a new type of nanocrystal assembly process that is driven by light and exciton directed.

PACS 81.16.-c · 81.07.-b · 62.23.St · 68.37.Ps · 78.67.-n

1 Introduction

Assembly or alignment of nanocrystals of numerous materials has been shown to be important for "tuning" useful material properties. To date, assembly of nanostructured materials has been achieved by the Langmuir Blodgett method [1–3], liquid crystalline assemblies [4–7] and, one-dimensional nanostructures dispersed in solution, by microfluidic [8, 9] chemical [10, 11], biochemical [12–15], and electric field alignment [16, 17]. Nanoparticle nanotubes (NPNT) is the recent class of self-assembled nanocrystals as tubes. Formation of such acicular nanoparticle assembly as tubes has been demonstrated [18, 19] recently by Rubinstain et al. and their alignment [20] by Zamborini et al. The Monte Carlo simulation by Kuon et al. shows self-assembly of polystyrene particles under illumination with laser light [21]. However, the assembly of nanocrystals of any material through irradiation by an incoherent visible light source is unknown in the literature, either theoretically or experimentally.

The work deals with fabrication of assembled nanostructures from the pre-synthesized nanocrystal building blocks, through the optical means of exciton formation and dissociation. It has been demonstrated that Li_xCoO_2 nanocrystals assemble into an acicular architecture, upon prolonged exposure to ultraviolet-visible radiation emitted from a 125 W mercury vapor lamp, through intermediate excitation of excitons. Furthermore, it has been shown that such assembly occurs in nanocrystals, initially anchored to substrate surface such as fused quartz in the form of thin films. Zunger et al. have shown [22] theoretically that exciton dissociation, i.e., the dissociation of an electron–hole pair localized in one quantum dot, and placing the electron and the hole in different dots leads to polarization effects in CdSe nanocrystals. Exciton dissociation and subsequent screened Coulomb attraction between the electron and the hole in different dots eventually lead to the formation of an acicular assembly. The disappearance of exciton bands due to Li_xCoO_2

M. Das (✉) · R. Ranjith · S.B. Krupanidhi · S.A. Shivashankar
Materials Research Centre, Indian Institute of Science, Bangalore 560012, India
e-mail: mahua@mrc.iisc.ernet.in

C. Bittencourt · J.J. Pireaux
LISE Laboratory, University of Namur, 61, Rue de Bruxelles, 5000 Namur, Belgium

phase in the optical spectrum of the irradiated film comprising acicular structure, as will be shown, supports this mechanism. The results demonstrate how nanocrystals of semiconducting and even some insulating materials with band gaps appropriate for excitation of excitons at specific optical wavelengths can be assembled to unusual nanoarchitectures through illumination with incoherent light sources. The fabrication approach or protocol, adopted in the present case, reduces significantly the number of critical processing steps involved in controlling the nanocrystal assembly process through a chemical route. It is anticipated that this novel approach of assembly in nanocrystals through optical means may be a starting point to developing a more effective, yet simpler way towards the generation and control of assembly in various nanocrystalline materials.

2 Experimental details

2.1 Synthesis

Hexagonal Li_xCoO_2 nanocrystals were obtained on quartz substrate by the sol–gel process, followed by thermal annealing at 440°C. The coating solution was prepared as follows: 1.5 g of $Co(NO_3)_2{\cdot}6H_2O$ was dissolved in 12 ml of distilled water, into which 3 ml of 1-aziridine ethanol was added and shaken, and was allowed to cool to room temperature. Into this mixture, 4 ml of 30% liquor ammonia was added and shaken and, finally, 0.21 g of $LiOH{\cdot}H_2O$ was added. The metallic Co:Li ratio in the reaction mixture was 1:1. The reaction mixture was stirred for 7 hours at room temperature to obtain a dark violet solution. The solution was then aged overnight and the solution was then spin-coated on fused quartz at room temperature under the following conditions, duration—2 min, number of coating—5. The coated substrate was dried overnight at room temperature, pre-fired at 150°C for 30 minutes (to remove the solvents), subsequently heated to 460°C, and then fired at 440°C for 45 minutes under static air. A shining, golden-colored film was obtained on fused quartz. The thermally annealed films were then irradiated using a 125 W mercury vapor lamp initially for 24 hours and subsequently for 72 hours.

2.2 Measurements

X-ray diffraction patterns for the films were recorded using a Phillips (PANalytical) X'Pert Pro diffractometer at angles of incidence between 10–80 degrees using a highly sensitive X'celerator detector. XRD was also carried out at grazing incidence (1°) using a highly sensitive and surface specific collimated beam detector. Samples for transmission electron microscopy were prepared by placing a drop of dispersion of film fragments in acetone onto carbon coated copper TEM grid. The TEM samples were examined using a JEOL 300 X microscope and a Technai microscope, for low-magnification and high-magnification imaging, respectively. Scanning electron microscopy was performed using a field emission scanning electron microscope (FESEM). The composition of the films was determined by X-ray photoelectron spectroscopy. Ultraviolet–visible spectroscopy was carried out on a Cintra-40 spectrometer, NIR spectra of the films were recorded on a Perkin Elmer Spectrum GX spectrometer.

3 Structural and compositional characterization

3.1 Grazing incidence X-ray diffraction (GIXRD) study

In the diffraction pattern (obtained at the grazing incidence angle of 1°) of the as-grown film (Fig. 1(a)), the peaks (marked by a) at $2\theta = 18.49°$, 37.3°, 44.4° correspond to the phase $Li_{x(x=0.62)}\ CoO_2$ (JCPDS-ICDD file no 37-1163); while the peak (marked by b) at $2\theta = 35.1°$ and the one at $2\theta = 45.2°$ correspond to the d-spacing of 2.55 Å

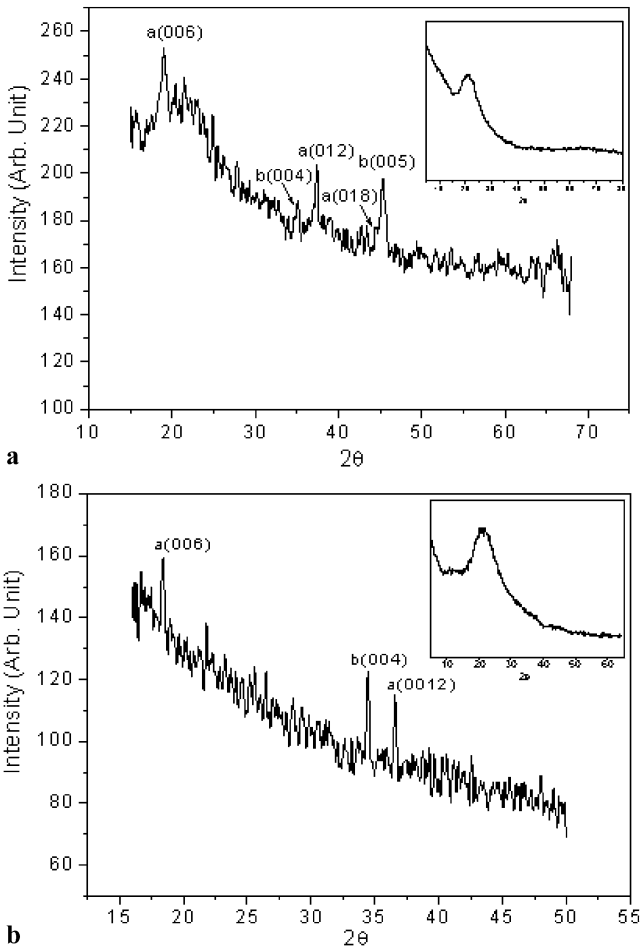

Fig. 1 XRD patterns of the film on fused quartz, (**a**) as-grown, (**b**) irradiated for 72 hours

and 2.04 Å, representing, respectively, the (004) and (005) planes of the LiC_{24} phase (JCPDS-ICDD File No. 35-1047). The diffraction pattern obtained at angles of incidence between 10 and 70° (shown as inset in Fig. 1(a)) shows no peak due to the film, but a broad hump between $2\theta = 16-27°$ due to the amorphous substrate, quartz. Similarly in the GIXRD pattern of the irradiated film (Fig. 1(b)), the peaks (denoted by a) at $2\theta = 18.4°$, 36.6° correspond to the $Li_{x(x=0.62)}CoO_2$ phase; the peak (denoted by b) at $2\theta = 34.44°$ corresponds to the lithium intercalated graphite phase, LiC_{24}. The diffraction pattern obtained at angles of incidence between 10 and 70° (shown as inset in Fig. 1(b)) does not show any peak due to the film.

The carbon clathrate C_{24} cage is formed through some kind of intermolecular ring expansion and elimination reaction between the 1-aziridene ethanolamine ligands in presence of aqueous ammonia at high temperature. Once the C_{24} carbon cage is formed, lithium gets intercalated into the cage to form LiC_{24}.

3.2 Scanning electron microscopy

Ultra-high resolution field emission scanning electron micrographs (FESEM) of the film grown on fused quartz are shown in Fig. 2, before and after irradiation. Figure 2(a) features the morphology of the thermally annealed (440°C), as-grown film before irradiation. The film, after irradiation for 72 hours, reveals the appearance of nanoparticles with long acicular structures, measuring ∼1.5–2 μm in length, wherein several nanobuilding blocks, each ∼14 × 14 nm, are assembled together to form what might be termed as a 'nano-babycorn' architecture (Fig. 2(f)). Figures 2(d)–(e) illustrate the partial lining up of such nanocrystals during the irradiation process. A 14 × 9 μm^2 area of the film consists of ∼20 such acicular structures, as evident from Fig. 2(c). Figure 2(f) reveals the array of several nanocrystals to form the acicular structure. The average particle sizes as estimated from the SEM micrographs are about 28 nm × 28 nm and 14 nm × 14 nm for the as-grown and the irradiated film, respectively.

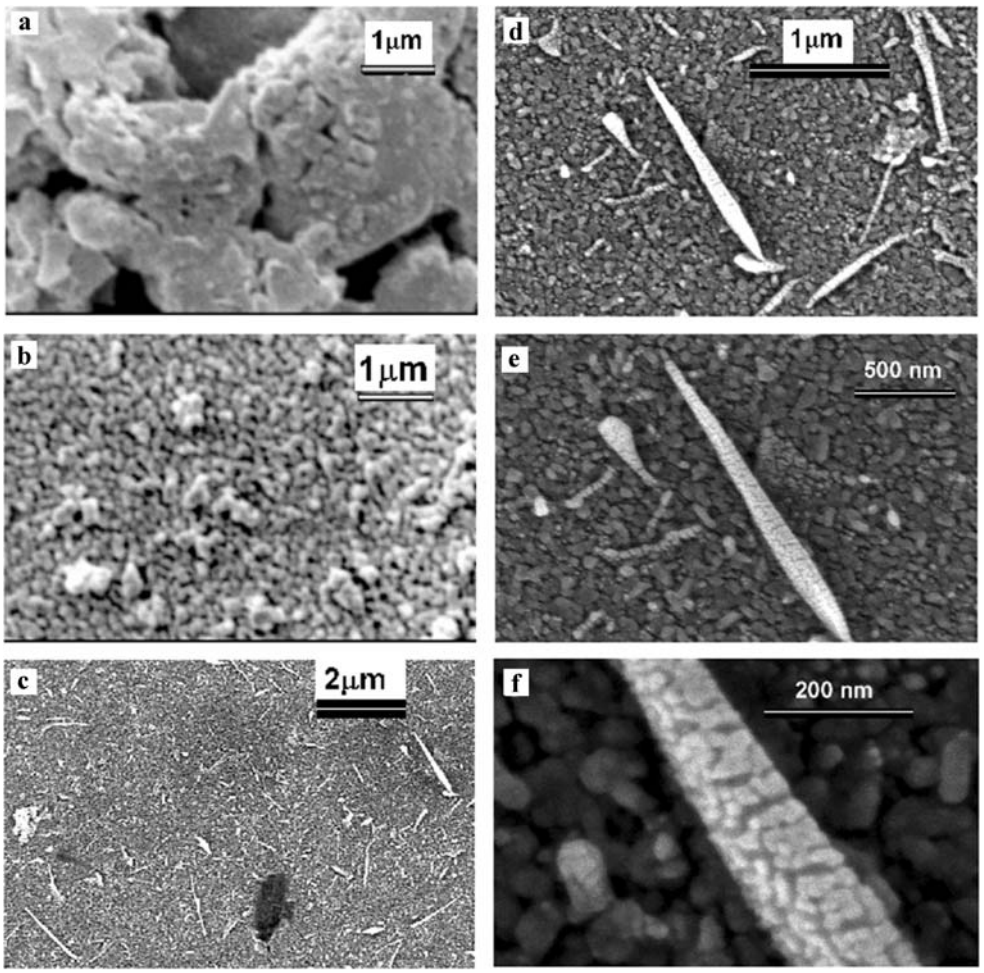

Fig. 2 Scanning electron micrographs of the films: (**a**) as-grown, (**b**) irradiated for 24 hours, (**c**, **d**, **e**, **f**) irradiated for 72 hours

3.3 Atomic force microscopy

Atomic force microscopy was carried out on the film comprising the acicular structure. Figure 3 shows the AFM micrographs recorded on the film at different magnifications. The maximum length of the acicular particle structure observed by AFM was about 8 µm (Fig. 3(b)). The alignment of nanocrystals is clearly visible in Fig. 3(c). It is noteworthy to observe the strong difference in contrast between the white acicular structure and the aligned nanocrystals. Such a strong contrast in color might be due to trapped charges along the acicular structure. In fact, a report in the literature [23] points out to a similar observation wherein a dark black-colored region that corresponds to trapped charge, observed through electrostatic force microscopic image (EFM), appears as a white region in a tapping-mode AFM image. Trapped charges are seen very prominently (as white regions) in Fig. 3(a). One way of checking whether the white region is indeed due to the trapped charge or to the length of the structure is to look at the smaller structures marked by

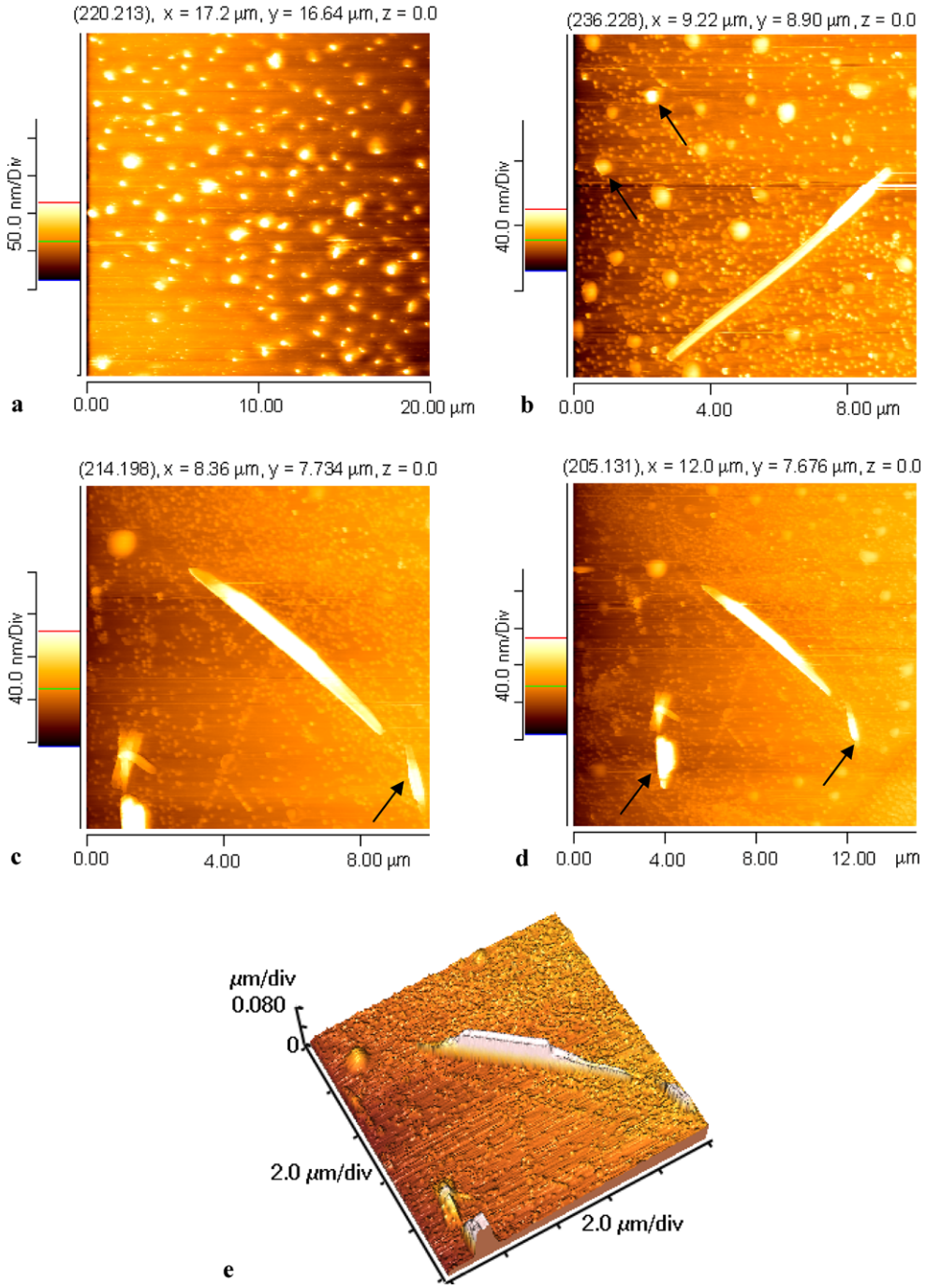

Fig. 3 AFM micrographs of the film comprising acicular structure

arrows in Figs. 3(c) and (d). Given the much smaller length of this structure, less than 80 nm, these structures should appear colored with tinge varying from brown to orange as evident from the scale bar in the images, if there were no trapped charges. The effect of a trapped charge is even more prominent in Fig. 3(b), wherein two particles (marked by arrows) of almost identical shape and size have two different colors, the one in which charge is trapped appears completely white. Figure 3(e) shows the three dimensional image of the two dimensional feature shown in Fig. 3(c). The image reveals the height of the acicular structure to be about 80 nm in and around the middle of the structure, and that the height decreases somewhat gradually away from the middle, on both sides along the length of the structure.

3.4 Electrostatic force microscopy

Electrostatic force microscopy (EFM) was carried out on the irradiated film in order to gain further mechanistic insight into the observed self-assembly process initiated by irradiation. EFM was performed on the film after 72 hours of irradiation, as shown in Fig. 4. EFM images show regions with dark red color and light green color in both "phase images" and "height images". The darker red region in the images may be attributed to the highly conducting particles in the film, and the light green region may be attributed to the relatively poorly conducting particles in it. Insulating particles appear completely white in EFM phase image, as found in the case of RuO_2/glass composite material [24]. Figure 4(a) shows the images recorded with varying tip bias (1 and 3 V), at a constant height of 150 nm. With increase in the bias, the EFM signal becomes stronger. Figure 4(b) shows that with increase in the lift height the EFM signal reduces. Both of these images show completely dark regions which suggest trapping of charge in these regions.

Figure 5 shows the EFM images recorded at different regions of the film. It is noteworthy (Fig. 5(a)) that, in the normal tapping mode phase image, there is a sharp gradient in the contrast along the cross-section of the acicular structure, which indicates an electrical field gradient across the surface of the elongated tube. This suggests charge induction and polarization by the charged particles. In the height image recorded at a tip bias of 3 V and lift height of 100 nm, (Fig. 5(b), bottom-left), a strong color contrast was observed; the nearly white region on the rod-type structure corresponds to the trapped charge. The localized charge can be distinguished by its nearly spherical shape, as opposed to grainy appearance of the nanoparticles. It is to be noted that, in the images (top left and bottom left in Fig. 5(b)), the color fades away from white to green, from the center towards the periphery because of charge dissipation.

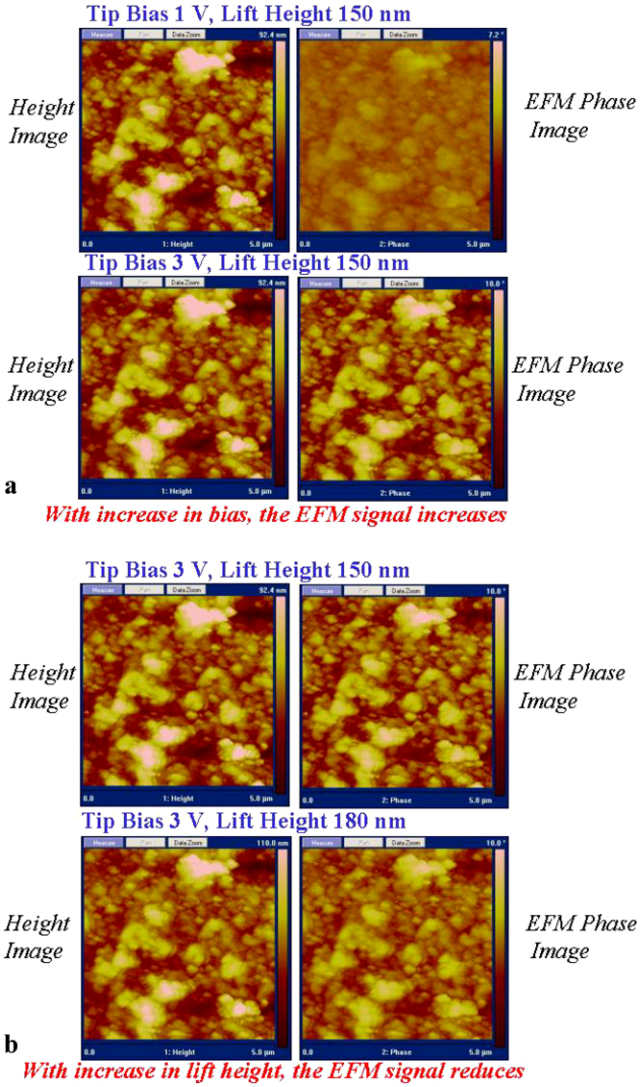

Fig. 4 EFM micrographs of the film comprising acicular structures

3.5 Transmission electron microscopy

Transmission electron microscopy was carried out in order to obtain further insight into the self-assembled nanostructure and the corresponding crystalline phases. Figures 6(a, b, c) feature the TEM images of the as-grown film, and Figs. 6(d, e, f) show those of the irradiated film. Figures 6(a) and (b) show the low-magnification TEM micrographs of the as-grown and the irradiated film, respectively; the corresponding SAED patterns are shown as the inset of these figures. The low–magnification TEM image (Fig. 6(a)) of the as-grown film reveals randomly distributed crystallites, typically about 50–80 nm in length. The d-spacing, as calculated from the image as well as from the fast Fourier transforms (FFT's), shown as the inset, is 4.8 and 4.85 Å for the as grown (Fig. 6(b)) and the irradiated film (Fig. 6(e)), respectively. The calculated values of d-spacings were compared with 2000 JCPDS-ICDD file No. 37-1163, and were

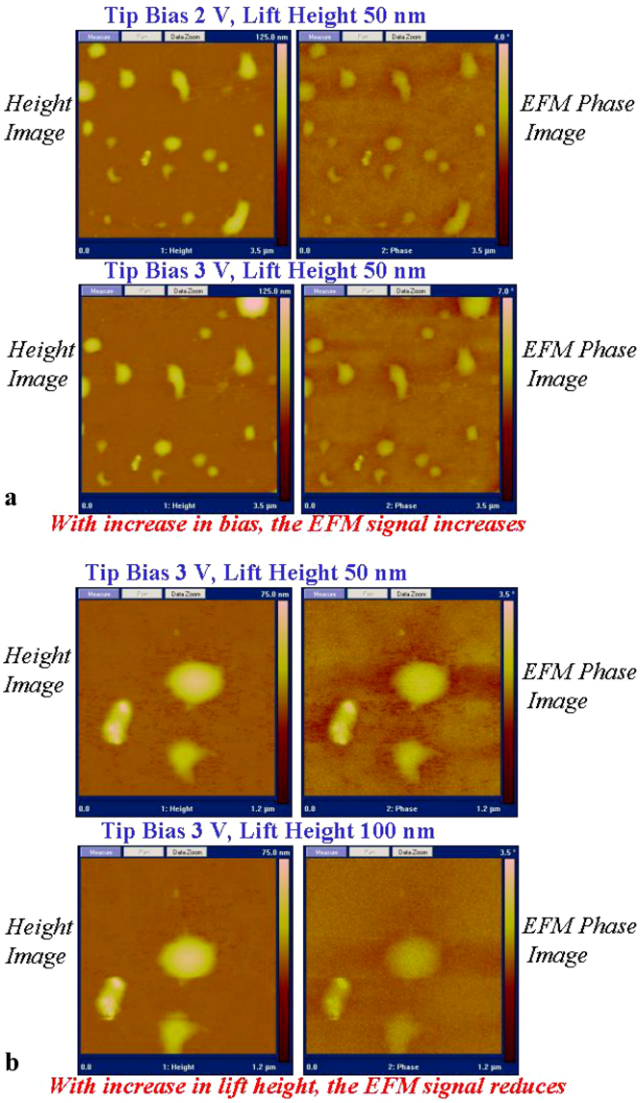

Fig. 5 EFM micrographs of the film comprising acicular structures at a different region

matched with that reported for (006) planes of hexagonal $Li_{0.62}CoO_2$ phase. Thus, it is inferred from the HRTEM study that both the as-grown and the irradiated film comprise hexagonal $Li_{0.62}CoO_2$ phase (Figs. 6(b) and (e)). High-resolution transmission electron micrograph of the as-grown (Fig. 6(c)) and the irradiated (Fig. 6(f)) film recorded at a different region of the film show crystallites with d spacing of 2 Å, this corresponds to the d spacing between (018) planes of $Li_{0.62}CoO_2$ phase.

It was not possible to distinguish between the hexagonal $Li_{0.62}CoO_2$ and the LiC_{24} crystallites based on HRTEM, However, the low-magnification images reveal many light grey needle-shaped crystallites along with black ones, of which the former most likely corresponds to lithium—intercalated graphite LiC_{24} phase.

3.6 X-ray photoelectron spectroscopy

X-ray photoelectron spectroscopy was carried out on the as-grown and the irradiated films on quartz substrate, in order to get insight into the chemical composition and the oxidation state of the elements present in the films. Since all the samples exhibited charging effect, the spectra presented here are corrected for this. To do this, we assumed a constant O1s binding energy of 529.4 eV as a reference. Figure 7 depicts the XPS spectra of the as-grown film on quartz, the binding energies which correspond to the components of the peaks are shown as the inset of each figure.

The Co2p peak can be decomposed into six components (Fig. 7(a)), of which the ones at binding energies of 780.19 eV and 795.23 eV are due to Co^{3+} ions, whereas the ones at 782.22 eV and 797.41 eV are due to Co^{4+} ions. The binding energy difference of 9.56 eV between the component at 780.19 eV and the satellite peak at 789.75 eV reveals the existence of Co^{3+} ions in the same environment as in $LiCoO_2$.

The O1s peak can be decomposed into three components (Fig. 7(b)). The components at 529.4 eV and 531.09 eV are attributed to the O^{2-} ions of the crystal structure. The component at 532.72 eV is due to the presence of OH^- species in the film.

The Li1s peak can be decomposed into two components (Fig. 7(c)). The symmetric one at binding energy of 54.14 eV is due to the Li located in the octahedral environment, the reported value of octahedrally surrounded Li in $Li_{0.62}CoO_2$ phase is 54 eV [25]. The one at binding energy of 60.67 eV is due the lithium intercalated in graphite, i.e., LiC_{24}. A satellite component of the Li1s peak was observed at 62.53 eV, at 1.8 eV higher binding energy above the main line in Li1s XPS due to LiC_{24}; this satellite component of the Li1s peak is the result of considerable charge transfer from Li to graphite conduction band [26]. This causes disappearance of band gap and overlap of HOMO and LUMO in LiC_{24} near Fermi energy. Creation of a deep localized hole in the process of X-ray photoemission from metals is followed by a drastic rearrangement of the surrounding electrons in the Fermi sea [27]. This rearrangement in which low kinetic energy electron–hole pairs are produced gives rise to a low kinetic energy (i.e., higher binding energy) tail in the hole spectral density. The case in which the hole potential is switched on instantaneously (the sudden or impulse limit) the asymmetric lines shapes are skewed towards high binding energy (low kinetic energy). Another satellite peak appeared at 70.63 eV. Penn reported [28] that the enhancement of satellite at a photon energy of 67 eV is related to the photoexcitation of a 3p core electron to an empty d state for metallic Ni. The photoexcitation is followed by an Auger process in which a d electron fills the core hole while another

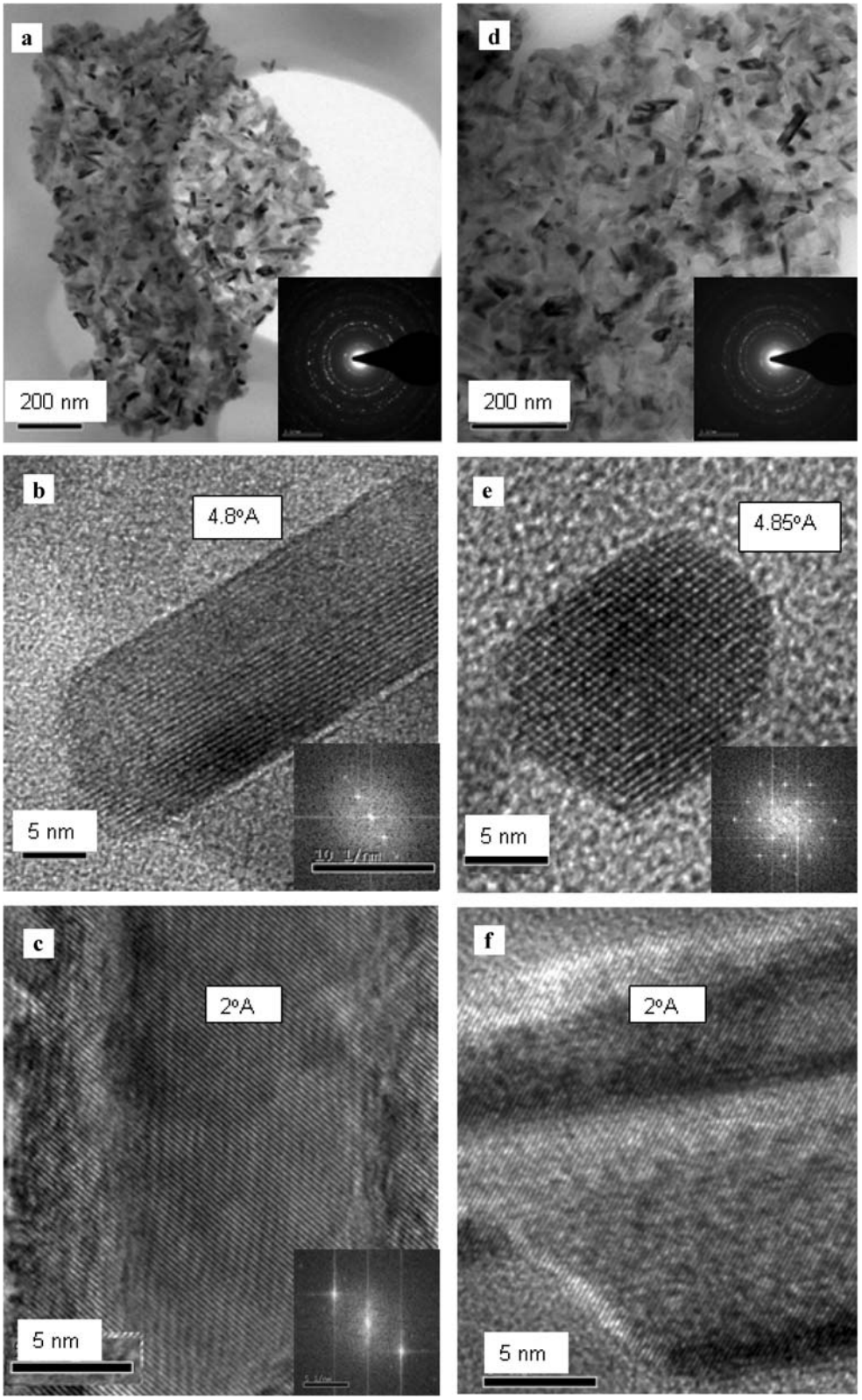

Fig. 6 Transmission electron micrographs of the film: (**a**–**c**) as grown; (**d**–**f**) irradiated

d electron is excited to a higher energy. If the two d holes produced in the Auger process are left in a virtual bound state the excited electron will have an energy corresponding to the satellite. A similar photoexcitation of electron from core level to empty d level and subsequent d–d transition takes place in the Li_xCoO_2, which results into bound hole pair at the 3d level and which accounts for the satellite peak observed at 70.63 eV.

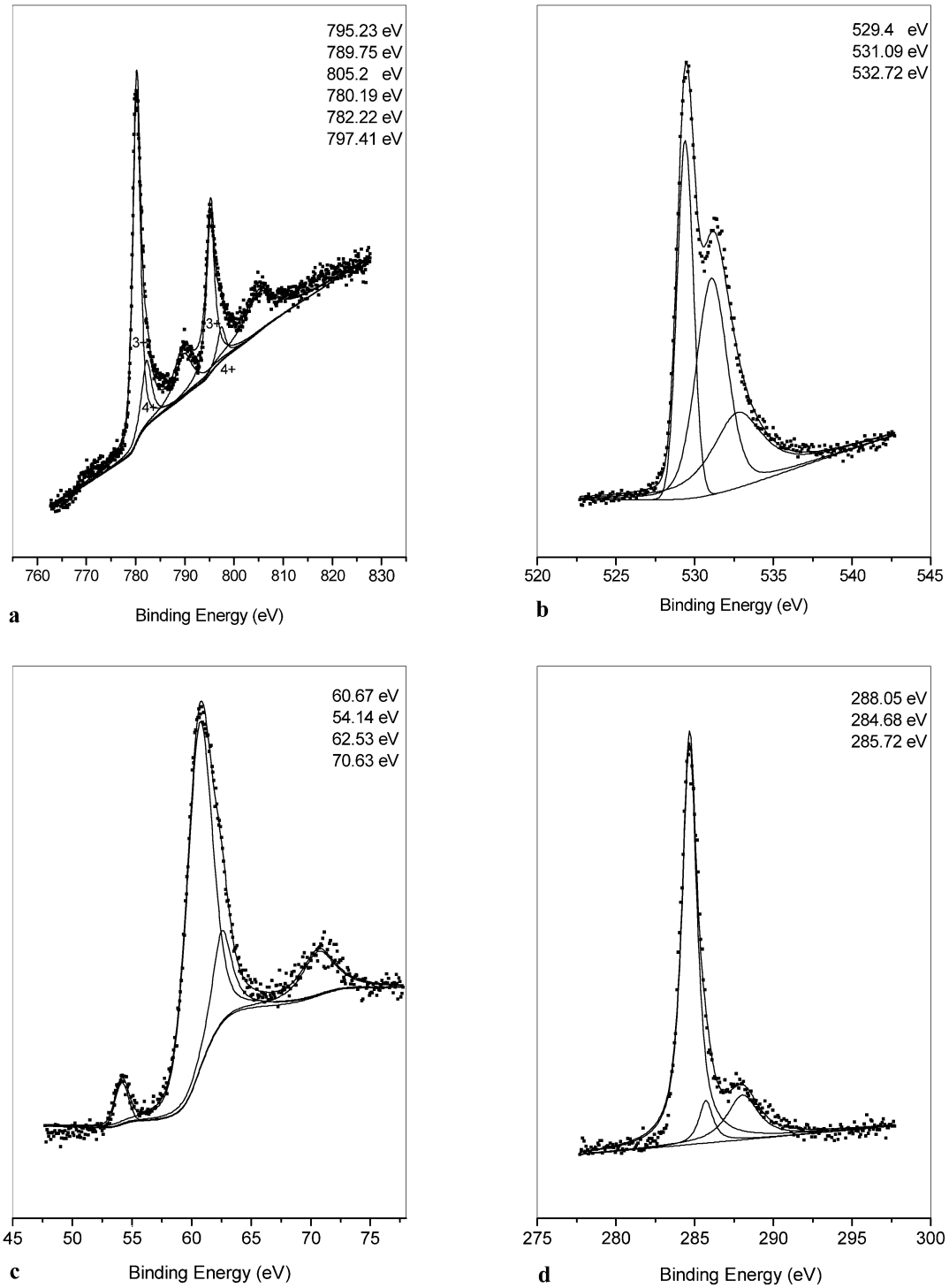

Fig. 7 XPS of the as-grown film on quartz: (**a**) Co2p, (**b**) O1s, (**c**) Li1s, and (**d**) C1s

The C1s peak consists of three components as shown in Fig. 7(d). The one at 284.68 eV is due to the graphite intercalated by lithium. In the lithium intercalated by graphite, the C1s binding energy increases (for pure graphite C1s line appears at 284.4 eV), which could be explained on the basis of charge transfer from lithium to the graphite conduction band. The change in binding energy is in part due to the screening of the core hole by the conduction electrons in lithium graphite [26]. The component at 285.72 eV is due to amorphous carbon and hydrocarbon C–H species. The one at 288.05 eV is due to the presence of C–O species.

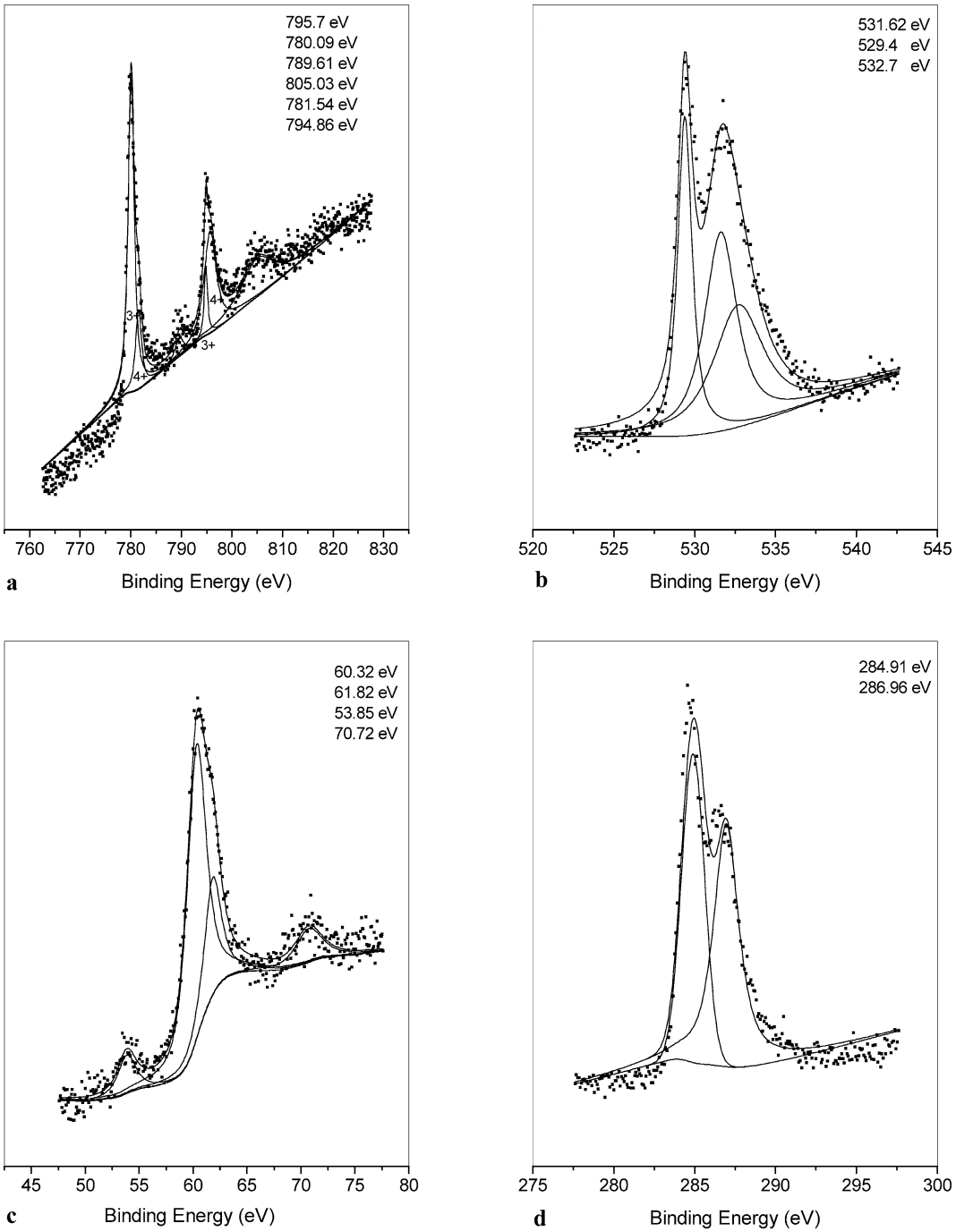

Fig. 8 XPS of the irradiated film on quartz: (**a**) Co2p, (**b**) O1s, (**c**) Li1s, and (**d**) C1s

Figure 8 illustrates the XPS spectra recorded on the irradiated film; the binding energies which correspond to the components of the peaks are listed.

The Co2p peak can be decomposed into six components (Fig. 8(a)), of which the ones at binding energies of 780.09 and 794.86 eV are due to Co^{3+} ions, whereas the ones at 781.54 and 795.7 eV are due to Co^{4+} ions.

The O1s peak can be decomposed into three components (Fig. 8(b)). The component at 529.4 eV is attributable to the O^{2-} ions of the crystal structure. The one at 531.62 eV may be attributed to presence of C=O species in the films. The component at 532.7 eV is due to the presence of OH^- species in the film.

The Li1s peak can be decomposed into two components (Fig. 8(c)). The one at binding energy 60.32 eV is due

the lithium-intercalated graphite, i.e., LiC_{24}. The symmetric one at binding energy of 53.85 eV is due to the Li located in the octahedral environment, in $Li_{0.62}CoO_2$. The peak at 70.72 eV is due to an electronic transition from core to d level and subsequent d–d transition and formation of bound hole pair in Li_xCoO_2 as described before.

The C1s peak consists of two components as shown in Fig. 8(d). The one at 284.91 eV is due to the graphite intercalated by lithium. The component at 286.96 eV is due to the presence of C=O species in the film.

The relative elemental concentrations of the films were calculated, and were found to be as follows: C 20%, Co 10%, O 10%, Li 60% for the as-grown film; C 20%, Co 5%, O 10%, Li 65% for the irradiated film. Lithium is present as intercalated in graphite and doped in $Li_{x(x=0.62)}CoO_2$ in the films. The interesting point to note here is that there is a 5% decrease in the Co concentration and a 5% increase in the lithium concentration in the irradiated film. XPS is sensitive to the first 50 Å of the film; this suggests selective migration or diffusion of lithium atom/ion from underneath the surface to the surface of the film upon irradiation.

Interesting and useful insights towards photoexcitation mechanism can be obtained upon comparative analysis of the Co2p peak of the non-irradiated to that of the irradiated one (Fig. 9). Remarkable difference was observed in the peak position, shape and width of the components due to Co^{4+}. The component at 782.22 eV in the Co2p peak of the un-irradiated one showed a binding energy shift of 0.68 eV towards lower binding energy in the irradiated one; the component at 797.41 eV of the unirradiated film showed a shift of 1.71 eV towards lower binding energy in the irradiated one. The area of the component at 795.7 eV of the irradiated film is larger than that of the component at 797.41 eV of the un-irradiated film. This suggests ionization of Co^{3+} to Co^{4+} upon irradiation. The shift of peak positions towards lower binding energy side in the irradiated film is caused by the descreening of the core electrons by the 3d-band holes created by ionization of Co^{3+}.

Carvalho et al. have shown [29] that N1s binding energy values decrease for CN_x materials when the molecule is embedded in a polarizable medium. This is consequence of the increased stabilization energy of the core hole state interacting with the polarization charges, compared to the neutral state. The L1s binding energy decreases by 0.25–0.35 eV upon irradiation. Upon ionization of Co^{3+} to Co^{4+}, the Co^{4+} atoms induce charges on nearby Li^+. The change in the chemical environment thus affects the interatomic transition determining core-hole lifetime in Li^+.

C1s binding energy due to lithium intercalated graphite showed an increase of 0.23 eV upon irradiation. To account for this increase, charge transfer from Co 3d band to graphite conduction band due to ionization of Co^{3+} to Co^{4+} is a likely possibility. Thus, extra electrons in the graphite conduction band provide additional screening to the core hole, which leads to observed increase in binding energy.

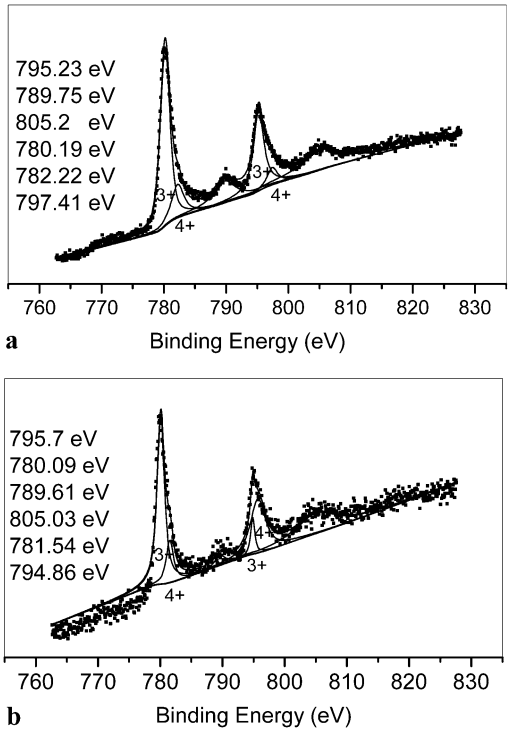

Fig. 9 XPS of Cp2p (**a**) as-grown un-irradiated film and (**b**) irradiated one

4 Mechanistic study of electromagnetic irradiation induced assembly through optical spectroscopy

4.1 Ultraviolet–visible spectroscopy

The self-assembly process of nanocrystals has been investigated by ultraviolet–visible (UV–vis, 300–800 nm) spectra recorded in the absorbance mode. The spectrum of the as-grown film shows a broad and weak absorption band at 474 nm in the visible region (Fig. 10(a)). The optical spectrum of the film after irradiation for 24 hours shows the appearance of additional bands both in the ultraviolet and the visible regions; three bands at 442, 452, and 502 nm were observed in the visible region of the spectrum (Fig. 10(b)). The excitation bands in the visible region disappear in the spectrum of the film upon irradiation for 72 hours (Fig. 10(c)).

The band at 474 nm in the optical spectrum of the as-grown film on quartz corresponds to absorption of photons of energy 2.62 eV. $LiCoO_2$ is semiconducting with a band gap of 2.7 eV, while Li_xCoO_2 at Li concentration below $x = 0.75$ is metallic or pseudometallic, implying that a metal–insulator transition occurs at the intermediate [30]. The simplest mechanism of semiconductor–metal transition

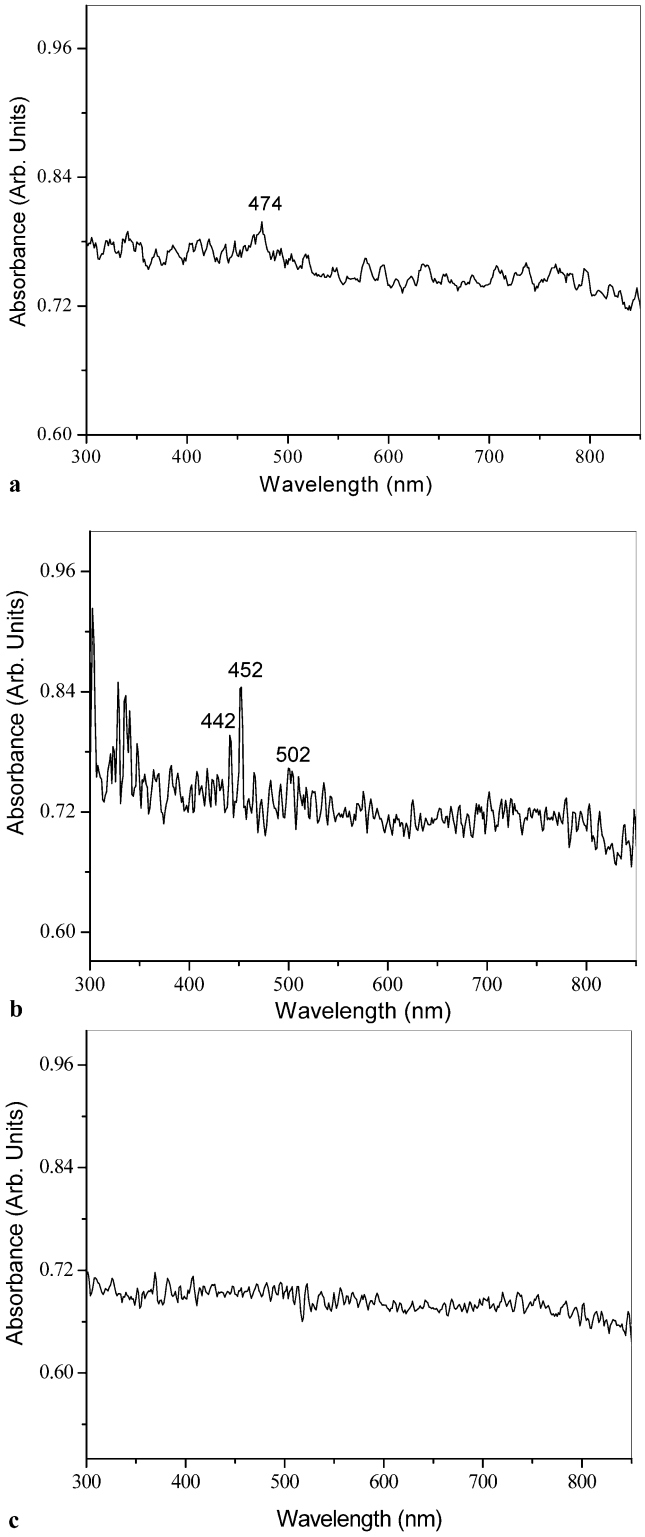

Fig. 10 Ultraviolet–visible spectra of the films: (**a**) as-grown, (**b**) irradiated for 24 hours, (**c**) irradiated for 72 hours

is ordinary band overlap, without accompanying crystalline symmetry changes [31]. If the material is a normal semiconductor, with a filled valence band separated from an empty conduction band by an energy gap which happens to decrease with increasing temperature, then, at a given temperature, the gap may vanish. This cannot happen to a direct gap when the bands are of same symmetry, due to the phenomenon of band repulsion. A more likely possibility is the vanishing of an indirect gap, in which case the transition is from a semiconductor to a semimetal. In this type of semiconductor–semimetal transition, the gap must pass through a region where its magnitude is extremely small, and the conditions are fulfilled for the formation of an excitonic insulator state [32]. The exciton energy corresponds to the Coulomb interaction between the valence band hole and the conduction band electron; in the optical spectrum obtained at room temperature, these bands often appear at wavelengths with optical absorption energy equivalent to the band gap of the material or less. The absorption energy calculated for absorption peak at 338 nm is 3.67 eV. The bands at 442 nm and 452 nm in the optical spectrum of the irradiated (24 hours) film correspond to the absorption of photons of energy 2.8 and 2.7 eV, respectively; the one at 502 nm corresponds to an absorption energy of 2.4 eV (Fig. 10(b)). The Co-3d bands of Li_xCoO_2 consist of three Co-t_{2g} (valence) and two Co-e_g (conduction) bands [33]. Kuriyama et al. have reported [34] the absorption peak at 2.1 eV associated with the transition of an electron from its valence band to the conduction band in $LiCoO_2$. The peaks in the visible region of the spectra, at 2.8 and 2.7 eV, are associated with the transition from E_F (in the t_{2g} valence band) to the conduction band (two e_g bands) of the $Li_{0.62}CoO_2$ phase. The absorption peaks at different values of energy may be attributed to the varying size/shape of the $Li_{0.62}CoO_2$ nanocrystals.

It is noteworthy that the peak at 502 nm is much wider and less intense than those at 442 and 452 nm. It is not clear whether this relatively low-intensity peak is associated with electronic transition in lithium-intercalated graphite or Li_xCoO_2 nanocrystallites. Holzwarth et al. have reported [35] calculation from first-principles of the electronic structure and band structure of the first, second, and third stage model graphite intercalation compounds, namely, LiC_6, LiC_{12}, and LiC_{18}. The typical bandgap of these pi-electron metals ranges between 1.3 and 1.6 eV, comparable to that of pure graphite, which rules out the possibility of the electronic transition from E_F to the conduction bands occurring in the visible range. It is likely that the photoionization of Co (3+) to Co (4+) leads to an intermediate band structure, which might be the origin of this less intense peak. Thus, photoionization of d-electron, preceded by t_{2g} to e_g electron transition, leaves a bound hole pair in the d-band; formation of this bound hole pair is crucial in the excitonic dissociation at a later stage.

It is crucial to note that the optical spectrum of the film comprising the acicular array structures does not show (Fig. 10(c)) any strong absorption peak in the ultraviolet visible region, which may be attributed to exciton dissociation

that would have already taken place in the film irradiated for 72 hours. It is proposed that the observed assembly process occurs through intermediate formation of excitons (revealed in the spectrum of the film irradiated for 24 hours) and their subsequent dissociation, as illustrated in Fig. 10. Zunger et al. have shown [22] theoretically that a screened Coulomb interaction occurs between electrons and holes in different quantum dots and polarization effects in CdSe nanocrystals. The dissociation energy decreases as the inter-dot distance decreases and the dielectric constant of the medium increases. The bandgap of CdSe is comparable to that of Li_xCoO_2, and ranges between 2.0 and 2.2 eV. The observation of the disappearance of exciton bands in the optical spectrum of the irradiated (72 hours) film comprising the acicular tubular structure is consistent with this mechanism.

The phenomenon of a photoexcited electron escaping a nanocrystal has been observed previously for II–VI semiconductors. In II–VI semiconductors, the hole has a large effective mass, while the electron is comparatively light. Therefore, in a nanocrystal, the hole tends to be localized, while the electron is much more delocalized with a non-negligible fraction of the electron density outside the crystal [36].

4.2 Near- and mid-infrared spectroscopy

Infrared (IR) spectra of the films on the Al and fused quartz substrates were obtained in the specular reflectance mode, at grazing incidence of 75°, for the as-grown and the irradiated films. The spectra were averaged over 256 scans and were normalized against the background spectrum of a silver mirror in order to obtain the absolute reflectance. During specular reflectance, only reflections directly from the film surface are considered, and transmission of radiation through the film is ignored. Therefore, the reflection dips observed in the specular reflectance spectra of the films correspond to absorption peaks by the film material.

Figures 11(a) and (b) show the near- and mid-infrared spectra for the as-grown and the irradiated films, respectively. Both the spectra showed the presence of O–H and C–H species in the films. The spectra can be divided into five regions in the NIR range, between 10,000 and 4000 cm^{-1}; denoted by I, II, III, IV, and V. Bands in these regions correspond to overtone and combinations bands of moieties such as O–H, C–H, and N–H [37].

Region I in Figs. 11(a) and (b) consists of reflection dips that correspond to the absorptions due to O–H 2nd overtone and C–H 3rd overtone. Region II comprises reflection dips that represent absorption due to O–H combination and C–H 2nd overtone. All the bands in Region III originate from C–H combination modes of vibrational–rotational excitation. The bands in Region IV and Region V correspond to O–H overtone and C–H 1st overtone, respectively.

Since the irradiation was carried out using a mercury vapor lamp, which emits radiation of frequencies that fall in the NIR region, spectral features in the mid-IR region have no direct relevance to the growth mechanism of the nanocrystal's assembly. However, the bands in the mid-IR region are considered the fingerprint or characteristic of the presence of specific organic functional moieties. To elucidate this point further, the sharp bands observed at 2967 and 2953 cm^{-1} for the as-grown and the irradiated film, respectively, confirm the presence of the C–H moiety. Similarly, the broad bands at 3689 and 3682 cm^{-1} indicate the presence of H_2O in the films.

5 Proposed mechanism of the nanocrystal's assembly

One mechanism consistent with the photoionization of an individual nanocrystal involves tunneling of the excited electron from one $Li_{0.62}CoOO_2$ nanocrystal into the adjacent $Li_{0.62}CoO_2$ nanocrystal, through the nearby metallic lithium-intercalated graphitic nanocrystals. The fact that a photoexcited electron escapes the nanocrystal is not entirely unexpected. What is surprising is that the photoinduced charge separation, or exciton dissociation, does not decay over time, rather the oppositely charged dots attract each other through screened Coulomb interaction, and thus they assemble together to form such an acicular architecture. The observation of the trapped charges in the AFM micrographs of the film comprising the acicular array structures is consistent with the proposed mechanism of exciton dissociation. Whether vibrational–rotational motions of the O–H and C–H species present in the film play any role in the exciton dissociation remains a question. It is noteworthy that the energy for exciton dissociation ranges between 100 and 300 meV for CdSe nanocrystals [22] with inter-dot distance of 3–4 nm; this energy falls in the NIR region.

Thus, the different steps involved in the growth of the acicular structures are as follows:

1. It begins with the photoexcitation of the electron from t_{2g}HOMO to e_gLUMO of Li_xCoO_2 and subsequent formation of an electron–hole pair or exciton.
2. On further illumination, the exciton dissociates and the screened Coulomb attraction between the hole and the electron in different dots leads to an alignment of charged species along a particular direction.
3. The charged nanocrystals polarize or induce charges on the adjacent nanocrystals.
4. Vibrational–rotational motions of the O–H and C–H species contribute to the translational movement of the surface nanocrystals anchored onto the substrates. Thus, the charged nanocrystals come close, align among themselves, and form the acicular array.

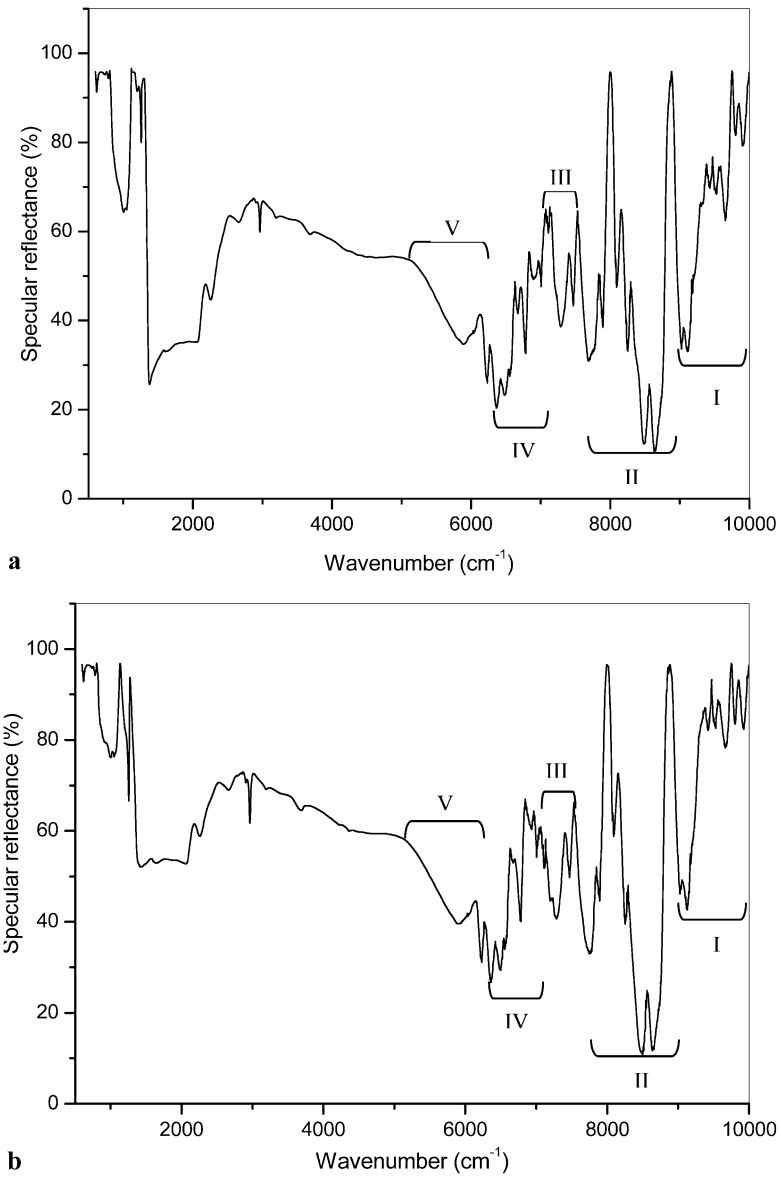

Fig. 11 Near- and mid-infrared spectra of the film (**a**) as-grown, (**b**) after 72 hours of irradiation

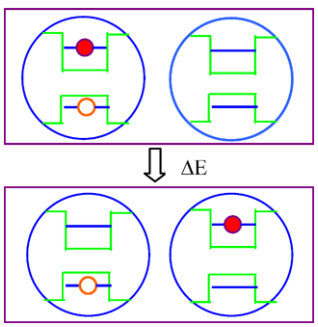

Fig. 12 Exciton dissociation in nanocrystals

Excitons and exciton dissociation (Fig. 12) are typically studied as the physical properties of semiconducting materials, rather than tools that provide control over nano-architecture. The results reported here provide clear evidence for the importance of exciton formation and dissociation in the growth process of Li_xCoO_2 'nano-babycorn' and nano-tubular architecture, from initially synthesized nanocrystals as building blocks. The work presents a new type of nanocrystal self-assembly process which is driven by irradiation and directed by excitons.

6 Summary and conclusions

Thin films comprising nanocrystalline $Li_{x(x=0.62)}CoO_2$ phase were grown using the sol–gel method. The nanocrystals organize into an acicular assembly under illumination with visible and NIR radiation. The as-grown film and the irradiated one were characterized by GIXRD, SEM, AFM, EFM, TEM. The SEM and TEM of the films reveal that the particle size distributions of these nanocrystals are quite

wide and only a few Li_xCoO_2 nanocrystals are assembled to rods. The mechanism of the observed self-assembly has been investigated by optical spectroscopy. The UV–visible spectroscopy of the as-grown and irradiated films showed a shift of 0.6 eV in the absorption peaks. The shift in the absorption peak from 2.1 eV ($LiCoO_2$) to about 2.7 eV ($Li_{0.62}CoO_2$) is most probably related to the different composition, and not to different shapes or sizes. The electromagnetic irradiation-induced self-assembly of Li_xCoO_2 nanocrystals is proposed to take place primarily through a mechanism involving exciton formation and subsequent dissociation.

Acknowledgements M.D. thanks Veeco-India nanotechnology laboratory, Bangalore for technical help with EFM measurements, and Mr. Amit Mandal (Institute Nanoscience Initiative, Indian Institute of Science) for technical help with HRTEM measurements.

References

1. D. Whang, S. Jin, Y. Wu, C.M. Lieber, Nano Lett. **3**, 1255 (2003)
2. F. Kim, S. Kwan, J. Akan, P. Yang, J. Am. Chem. Soc. **123**, 4360 (2001)
3. A. Tao, F. Kim, C. Hess, J. Goldberger, R. He, Y. Sun, Y. Xia, P. Yang, Nano Lett. **3**, 1229 (2003)
4. N.R. Jana, L.A. Gearheart, S.O. Obare, C.J. Johnson, K.J. Edler, S. Mann, C.J. Murphy, J. Mater. Chem. **12**, 2909 (2002)
5. L.-S. Li, A.P. Alivisatos, Adv. Mater. **15**, 408 (2003)
6. L.-S. Li, J. Walda, L. Manna, A.P. Alivisatos, Nano Lett. **2**, 557 (2002)
7. Y. Huang, X. Duan, Q. Wei, C.M. Lieber, Science **291**, 630 (2001)
8. B. Messer, J.H. Song, P.J. Yang, J. Am. Chem. Soc. **122**, 10232 (2000)
9. A. Gole, C.J. Orendorff, C.J. Murphy, Langmuir **20**, 7117 (2004)
10. B.R. Martin, S.K.St. Angelo, T.E. Mallouk, Adv. Funct. Mater. **12**, 759 (2002)
11. K.K. Caswell, J.N. Wilson, U.H.F. Bunz, C.J. Murphy, J. Am. Chem. Soc. **125**, 13914 (2003)
12. E. Dujardin, L.-B. Hsin, C.R.C. Wang, S. Mann, Chem. Commun. 1264 (2001)
13. B.R. Martin, D.J. Dermody, B.D. Reiss, M. Fang, L.A. Lyon, M.J. Natan, Adv. Mater. **11**, 1021 (1999)
14. J.K.N. Mbindyo, B.D. Reiss, B.R. Martin, C.D. Keating, M.J. Natan, T.E. Mallouk, Adv. Mater. **13**, 249 (2001)
15. C.A. Mirkin, R.L. Letsinger, R.C. Mucic, J.J. Storhoff, Nature **382**, 607 (1996)
16. P.A. Smith, C.D. Nordquist, T.N. Jackson, T.S. Mayer, B.R. Martin, J. Mbindyo, T.E. Mallouk, Appl. Phys. Lett. **77**, 1399 (2000)
17. O. Harnack, C. Pacholski, H. Weller, A. Yasuda, J.M. Wessels, Nano Lett. **3**, 1097 (2003)
18. M. Lahav, T. Sehayek, A. Vaskevich, I. Rubinstein, Angew. Chem. Int. Ed. Engl. **42**, 5576 (2003)
19. T. Sehayek, M. Lahav, R. Popovitz-Biro, A. Vaskevich, A. Rubinstein, Chem. Mat. **17**, 3743 (2005)
20. A.J. Mieszawska, F.P. Zamborini, Chem. Mat. **17**, 3415 (2005)
21. K. Ishii, T. Iwai, K. Inoue, Proc. SPIE **4598**, 80 (2001)
22. A. Franceschetti, A. Zunger, Phys. Rev. B **63**, 153304 (2001)
23. C.A. Huber, T.E. Huber, M. Sadoqi, L.A. Lubin, S. Manalis, C.B. Prater, Science **263**, 800 (1994)
24. R. Viswanathan, M.B. Heaney, Phys. Rev. Lett. **75**, 4433 (1995)
25. J.C. Dupin et al., Thin Solid Films **384**, 23 (2001)
26. E.G. Gal'pern, I.V. Stankevich, A.L. Chistykov, L.A. Chernozatonskii, Chem. Phys. Lett. **214**, 345 (1993)
27. J.W. Gadzuk, M. Šunjić, Phys. Rev. B **12**, 524 (1975)
28. D.R. Penn, Phys. Rev. Lett. **42**, 921 (1979)
29. A.C.M. Carvalho, M.C. dos Santos, J. Non-Cryst. Solids **338–340**, 254 (2004)
30. J. Molenda, A. Stoklosa, T. Bak, Solid State Ionics **36**, 53 (1989)
31. D. Alder, Rev. Mod. Phys. **40**, 714 (1968)
32. B.I. Halperin, T.M. Rice, Rev. Mod. Phys. **40**, 755 (1968)
33. M.T. Czyzyk, R. Potze, G.A. Sawatzky, Phys. Rev. B **46**, 3729 (1992)
34. K. Kushida, K. Kuriyama, Solid State Commun. **118**, 615 (2001)
35. N.A.W. Holzwarth, S.G. Louie, S. Rabii, Phys. Rev. B **28**, 1013 (1983)
36. D. Schooss, A. Mews, A. Eychmueller, H. Weller, Phys. Rev. B **49**, 17072 (1994)
37. B.G. Osborne, Near infrared spectroscopy in food analysis, in *Enclyclopedia of Analytical Chemistry*, ed. by R.A. Meyers (Wiley, New York, 1986)